Chapter 5

Modeling of Continuous Casting

Brian G. Thomas, Professor of Mechanical Engineering, University of Illinois

---

The high cost of empirical investigation in an operating steel plant makes it prudent to use all available tools in designing, troubleshooting and optimizing the process. Physical modeling, such as using water to simulate molten steel, enables significant insights into the flow behavior of liquid steel processes. The complexity of the continuous casting process and the phenomena which govern it, illustrated in Figs. 5.1 and 5.2, make it difficult to model. However, with the increasing

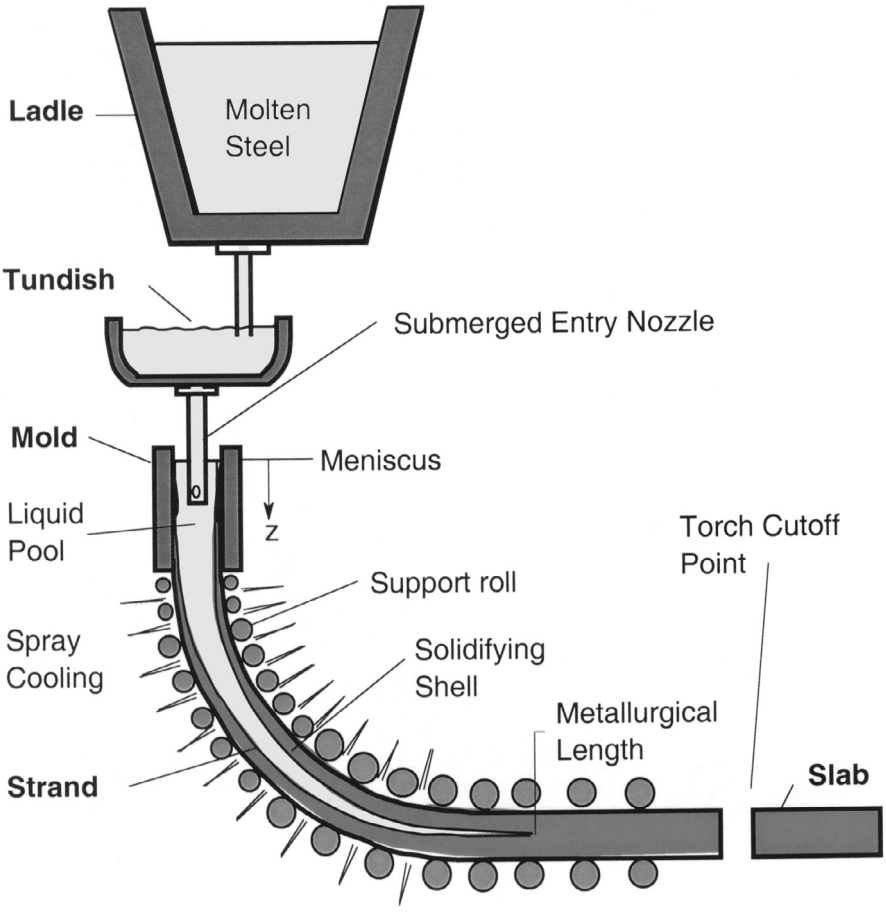

Fig. 6.1 Schematic of continuous casting process.

power of computer hardware and software, mathematical modeling is becoming an important tool to understand all aspects of the process.

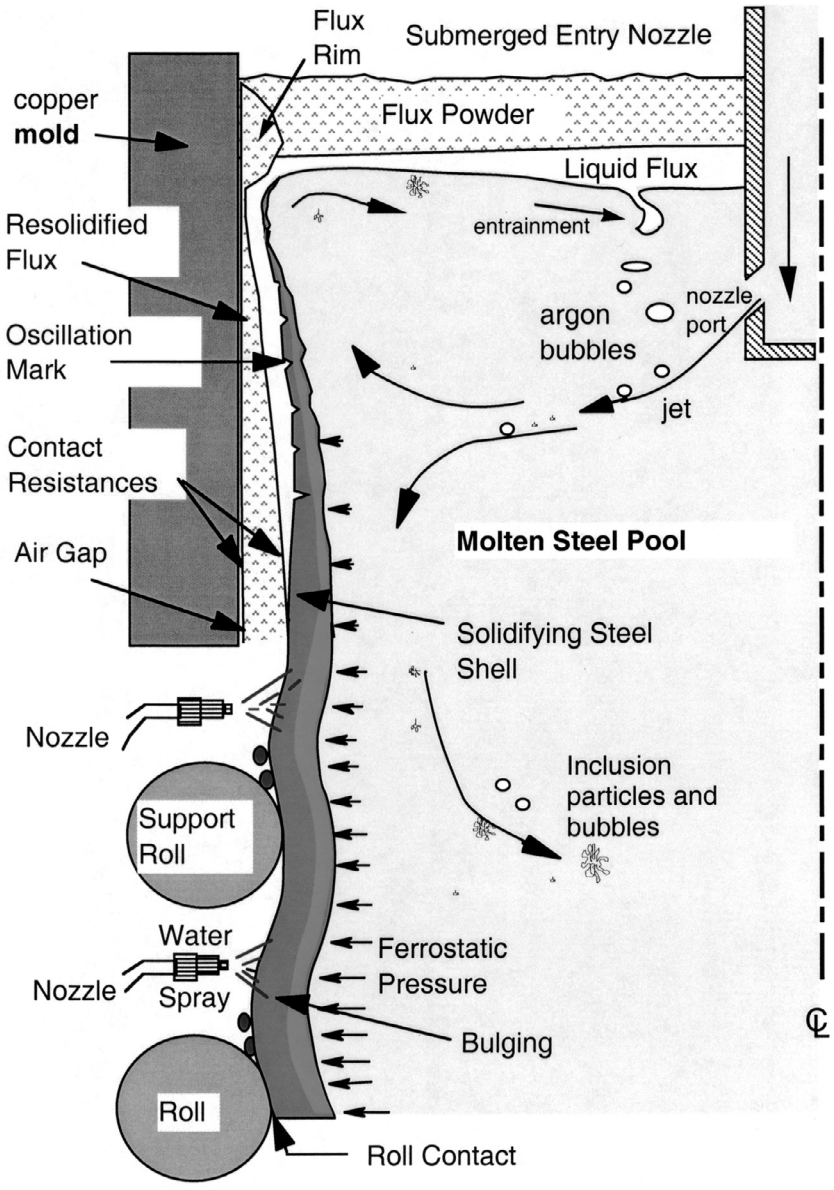

Fig. 5.2 Schematic of phenomena in the mold region of a steel slab caster.

5.1 Physical Models

Previous understanding of fluid flow in continuous casting has come about mainly through experiments using physical water models. This technique is a useful way to test and understand the effects of new configurations before implementing them in the process. A full-scale model has the important additional benefit of providing operator training and understanding.

Construction of a physical model is based on satisfying certain similitude criteria between the model and actual process by matching both the geometry and the force balances that govern the important phenomena of interest.[1–4] Some of the forces important to flow phenomena are listed in Table 5.1. To reproduce the molten steel flow pattern with a water model, all of the ratios between

the dominant forces must be the same in both systems. This ensures that velocity ratios between the model and the steel process are the same at every location. Table 5.2 shows some of the important force ratios in continuous casting flows, which define dimensionless groups. The size of a dimensionless group indicates the relative importance of two forces. Very small or very large groups can be ignored, but all dimensionless groups of intermediate size in the steel process must be matched in the physical model.

Table 5.1 Forces Important to Fluid Flow Phenomena.

Inertia	$\rho L^2 V^2$	L = length scale (m)
Gravity	$\rho g L^3$	V = velocity (m/s)
Buoyancy	$(\rho - \rho_p) g L^3$	ρ = fluid density (kg/m^3)
Viscous force	$\mu L V$	μ = viscosity (kg/m-s)
Thermal buoyancy	$\rho g L^3 \beta \Delta T$	g = gravity accel. = 9.81 m/s^2
Surface tension	σL	σ = surface tension (N/m)
		β = thermal exp. coef. (m/m-°C)
		ΔT = temperature difference (°C)
		p = particle of solid or gas

Table 5.2 Dimensionless Groups Important to Fluid Flow Phenomena.

Force Ratio	Definition	Name	Phenomena
$\frac{\text{Inertial}}{\text{Viscous}}$	$\frac{VL\rho}{\mu}$	Reynolds	Fluid momentum
$\frac{\text{Inertial}}{\text{Gravitational}}$	$\frac{V^2}{gL}$	Froude	Gravity-driven flow; Surface waves
$\frac{\text{Inertial}}{\text{Thermal buoyancy}}$	$\frac{V^2}{gL\beta\Delta T}$	Froude*	Natural convection
$\frac{\text{Inertial}}{\text{Surface Tension}}$	$\frac{\rho LV^2}{\sigma}$	Weber	Bubble formation; Liquid jet atomization

* Modified Froude number

An appropriate geometry scale and fluid must be chosen to achieve these matches. It is fortunate that water and steel have very similar kinematic viscosities (μ/ρ). Thus, Reynolds and Froude numbers can be matched simultaneously by constructing a full-scale water model. Satisfying these two criteria is sufficient to achieve reasonable accuracy in modeling isothermal single-phase flow systems, such as the continuous casting nozzle and mold, which has been done with great success. A full-scale model has the extra benefit of easy testing of plant components and operator training. Actually, a water model of any geometric scale produces reasonable results for most of these flow systems, so long as the velocities in both systems are high enough to produce fully turbulent flow and very high Reynolds numbers. Because flow through the tundish and mold nozzles are gravity driven, the Froude number is usually satisfied in any water model of these systems where the hydraulic heads and geometries are all scaled by the same amount.

Physical models sometimes must satisfy heat similitude criteria. In physical flow models of steady flow in ladles and tundishes, for example, thermal buoyancy is large relative to the dominant inertial-driven flow, as indicated by the size of the modified Froude number (Froude* in Table 5.2), which therefore must be kept the same in the model as in the steel system. In ladles, where velocities are difficult to estimate, it is convenient to examine the square of the Reynolds number divided by the modified Froude number, which is called the Grashof number. Inertia is dominant in the mold, so thermal buoyancy can be ignored there. The relative magnitude of the thermal buoyancy forces can be matched in a full-scale hot water model, for example, by controlling temperatures and heat losses such that $\beta\Delta T$ is the same in both model and caster. This is not easy, however, as the phenomena that govern heat losses depend on properties such as the fluid conductivity and specific heat and the vessel wall conductivity, which are different in the model and the steel vessel. In other systems, such as those involving low velocities, transients or solidification, simultaneously satisfying the many other similitude criteria important for heat transfer is virtually impossible.

When physical flow models are used to study other phenomena, other force ratios must be satisfied in addition to those already mentioned. For the study of inclusion particle movement, for example, it is important to match the force ratios involving inertia, drag and buoyancy. This generates several other conditions to satisfy, such as matching the terminal flotation velocity, which is:[5]

$$V_T = \frac{g(\rho - \rho_p)d_p^{\,2}}{18\mu(1 + 0.15\,\mathrm{Re}^{0.687})} \qquad \text{(Eq. 5.1)}$$

where:

V_T = particle terminal velocity (m/s),
ρ, ρ_p = liquid, particle densities (kg / m^3),
d_p = particle diameter (m),
μ = liquid viscosity (kg / m-s),
g = gravity accel. = 9.81 m/s^2,
Re = particle Reynold's number = $\rho V_T\, d_p / \mu$.

In a full-scale water model, for example, 2.5-mm plastic beads with a density of 998 kg/m^3 might be used to simulate 100-μm 2300 kg/m^3 solid spherical inclusions in steel because they have the same terminal flotation velocity (equation 5.1), but are easier to visualize.

Sometimes, it is not possible to match all of the important criteria simultaneously. For example, in studying two-phase flow, such as gas injection into liquid steel, new phenomena become important. The fluid density depends on the local gas fraction, so flow similitude requires additional matching of the gas fraction and its distribution. The gas fraction used in the water model must be increased in order to account for the roughly fivefold gas expansion that occurs when cold gas is injected into hot steel. Adjustments must also be made for the local pressure, which also affects this expansion. In addition to matching the gas fraction, the bubble size should be the same, so force ratios involving surface tension, such as the Weber number, should also be matched. In attempting to achieve this, it may be necessary to deviate from geometric similitude at the injection point and to wax the model surfaces to modify the contact angles, in order to control the initial bubble size. If gas momentum is important, such as for high gas injection rates, then the ratio of the gas and liquid densities must also be the same. For this, helium in water is a reasonable match for argon in steel. In many cases, it is extremely difficult to simultaneously match all of the important force ratios. To the extent that this can be approximately achieved, water modeling can reveal accurate insights into the real process.

To quantify and visualize the flow, several different methods may be used. The easiest is to inject innocuous amounts of gas, tracer beads or dye into the flow for direct observation or photography.

Quantitative mixing studies can measure concentration profiles of other tracers, such as dye with colorimetry measurement, salt solution with electrical conductivity, or acid with pH tracking.[4] For all of these, it is important to consider the relative densities of the tracer and the fluid. Accurate velocity measurements, including turbulence measurements, may be obtained with hot wire anemometry,[6] high-speed videography with image analysis, particle image velocimetry (PIV)[7, 8] or laser doppler velocimetry (LDV).[9] Depending on the phenomena of interest, other parameters may be measured, such as pressure and level fluctuations on the top surface.[10]

As an example, Fig. 5.3 shows the flow modeled in the mold region of a continuous thin-slab caster.[11] The right side visualizes the flow using dye tracer in a full-scale physical water model. This particular caster features a 3-port nozzle that directs some of the flow downward in order to stabilize the flow pattern from transient fluctuations and to dissipate some of the momentum to lessen surface turbulence. The symmetrical left side shows results from the other important analysis tool: computational modeling, which is discussed in the next section.

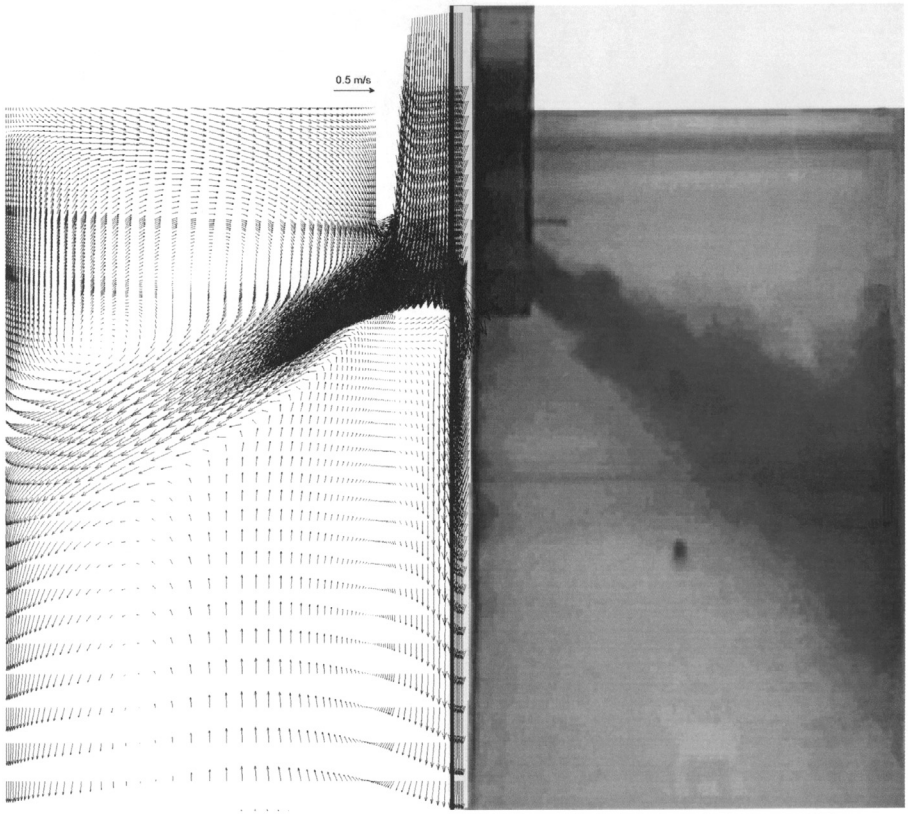

Fig. 5.3 Flow in a thin-slab casting mold visualized using (a) K-ε computer simulation and (b) water model with dye injection. *From Ref. 11.*

5.2 Computational Models

In recent years, decreasing computational costs and the increasing power of commercial modeling packages are making it easier to apply mathematical models as an additional tool to understand complex materials processes such as the continuous casting of steel. Computational models have the advantage of easy extension to other phenomena such as heat transfer, particle motion and two-phase flow, which is difficult with isothermal water models. They are also capable of more faithful

representation of the flow conditions experienced by the steel. For example, there is no need for the physical bottom that interferes with the flow exiting a strand water model, and the presence of the moving solidifying shell can be taken into account.

Models can now simulate most of the phenomena important to continuous casting, which include:

- fully-turbulent, transient fluid motion in a complex geometry (inlet nozzle and strand liquid pool), affected by argon gas bubbles, thermal and solutal buoyancies,
- thermodynamic reactions within and between the powder and steel phases,
- flow and heat transport within the liquid and solid flux layers, which float on the top surface of the steel,
- dynamic motion of the free liquid surfaces and interfaces, including the effects of surface tension, oscillation and gravity-induced waves, and flow in several phases,
- transport of superheat through the turbulent molten steel,
- transport of solute (including intermixing during a grade change),
- transport of complex-geometry inclusions through the liquid, including the effects of buoyancy, turbulent interactions, and possible entrapment of the inclusions on nozzle walls, gas bubbles, solidifying steel walls, and the top surface,
- thermal, fluid and mechanical interactions in the meniscus region between the solidifying meniscus, solid slag rim, infiltrating molten flux, liquid steel, powder layers and inclusion particles,
- heat transport through the solidifying steel shell, the interface between shell and mold (which contains powder layers and growing air gaps), and the copper mold,
- mass transport of powder down the gap between shell and mold,
- distortion and wear of the mold walls and support rolls,
- nucleation of solid crystals, both in the melt and against mold walls,
- solidification of the steel shell, including the growth of dendrites, grains and microstructures, phase transformations, precipitate formation, and microsegregation,
- shrinkage of the solidifying steel shell due to thermal contraction, phase transformations and internal stresses,
- stress generation within the solidifying steel shell due to external forces (mold friction, bulging between the support rolls, withdrawal, gravity), thermal strains, creep, and plasticity (which varies with temperature, grade and cooling rate),
- crack formation,
- coupled segregation, on both microscopic and macroscopic scales.

The staggering complexity of this process makes it impossible to model all of these phenomena together at once. Thus, it is necessary to make reasonable assumptions and to uncouple or neglect the less-important phenomena. Quantitative modeling requires incorporation of all of the phenomena that affect the specific issue of interest, so every model needs a specific purpose. Once the governing equations have been chosen, they are generally discretized and solved using finite-difference or finite-element methods. It is important that adequate numerical validation be conducted. Numerical errors commonly arise from too coarse a computational domain or incomplete convergence when solving the nonlinear equations. Solving a known test problem and conducting mesh refinement studies to achieve grid independent solutions are important ways to help validate the model. Finally, a model must be checked against experimental measurements on both

the laboratory and plant scales before it can be trusted to make quantitative predictions of the real process for a parametric study.

5.2.1 Heat Transfer and Solidification

Models to predict temperature and growth of the solidifying steel shell are used for basic design, troubleshooting and control of the continuous casting process.[12] These models solve the transient heat conduction equation,

$$\frac{\partial}{\partial t}(\rho H) + \frac{\partial}{\partial x_i}(\rho v_i H) = \frac{\partial}{\partial x_i}(k_{eff})\frac{\partial T}{\partial x_i} + Q \qquad \text{(Eq. 5.2)}$$

where:

$\partial/\partial t$ = differentiation with respect to time (s^{-1}),

ρ = density (kg/m^3),

H = enthalpy or heat content (J/kg),

x_i = coordinate direction, x, y or z (m),

v_i = velocity component in x_i direction (m/s),

k_{eff} = temperature-dependent effective thermal conductivity (W/m-K),

T = temperature field (K),

Q = heat sources (W/m^3),

i = coordinate direction index which, when appearing twice in a term, implies the summation of all three possible terms.

An appropriate boundary condition must be provided to define heat input to every portion of the domain boundary, in addition to an initial condition (usually fixing temperature to the pouring temperature). Latent heat evolution and heat capacity are incorporated into the constitutive equation that must also be supplied to relate temperature with enthalpy.

Axial heat conduction can be ignored in models of steel continuous casting because it is small relative to axial advection, as indicated by the small Peclet number (casting speed multiplied by shell thickness divided by thermal diffusivity). Thus, Lagrangian models of a horizontal slice through the strand have been employed with great success for steel.[13] These models drop the second term in equation 5.2 because velocity is zero in this reference frame. The transient term is still included, even if the shell is withdrawn from the bottom of the mold at a casting speed that matches the inflow of metal, so the process is assumed to operate at steady state.

Heat transfer in the mold region is controlled by:

- convection of liquid superheat to the shell surface,
- solidification (latent heat evolution in the mushy zone),
- conduction through the solid shell,
- the size and properties of the interface between the shell and the mold,
- conduction through the copper mold,
- convection to the mold-cooling water.

By far the most dominant of these is heat conduction across the interface between the surface of the solidifying shell and the mold, although the solid shell also becomes significant lower down. The greatest difficulty in accurate heat flow modeling is determination of the heat transfer across

this gap, q_{gap}, which varies with time and position depending on its thickness and the properties of the gas or lubricating flux layers that fill it:

$$q_{gap} = \left(h_{rad} + \frac{k_{gap}}{d_{gap}} \right) (T_{0shell} - T_{0mold}) \qquad \text{(Eq. 5.3)}$$

where:

q_{gap} = local heat flux (W/m^2),

h_{rad} = radiation heat transfer coefficient across the gap (W/m^2K),

k_{gap} = effective thermal conductivity of the gap material (W/mK),

d_{gap} = gap thickness (m),

T_{0shell} = surface temperature of solidifying steel shell (K),

T_{0mold} = hot face surface temperature of copper mold (K).

Usually, q_{gap} is specified only as a function of distance down the mold, in order to match a given set of mold thermocouple data.[14] However, where metal shrinkage is not matched by taper of the mold walls, an air gap can form, especially in the corners. This greatly reduces the heat flow locally. More complex models simulate the mold, interface, and shell together, and use shrinkage models to predict the gap size.[15–17] This may allow the predictions to be more generalized.

Mold heat flow models can feature a detailed treatment of the interface.[18–23] Some include heat, mass, and momentum balances on the flux in the gap and the effect of shell surface imperfections (oscillation marks) on heat flow and flux consumption.[23] This is useful in steel slab casting operations with mold flux, for example, because h_{rad} and k_{gap} both drop as the flux crystallizes and must be modeled properly in order to predict the corresponding drop in heat transfer. The coupled effect of flow in the molten metal on delivering superheat to the inside of the shell and thereby retarding solidification can also be modeled quantitatively.[23,24] Mold heat flow models can be used to identify deviations from normal operation and thus predict quality problems such as impending breakouts or surface depressions in time to take corrective action.

During the initial fraction of a second of solidification at the meniscus, a slight undercooling of the liquid is required before nucleation of solid crystals can start. The nuclei rapidly grow into dendrites, which evolve into grains and microstructures. These phenomena can be modeled using microstructure models such as the cellular automata[25] and phase field[26] methods. The latter requires coupling with the concentration field on a very small scale so is very computationally intensive.

Below the mold, air mist and water spray cooling extract heat from the surface of the strand. With the help of model calculations, cooling rates can be designed to avoid detrimental surface temperature fluctuations. Online open-loop dynamic cooling models can be employed to control the spray flow rates in order to ensure uniform surface cooling even during transients, such as the temporary drop in casting speed required during a nozzle or ladle change.[27]

The strand core eventually becomes fully solidified when it reaches the "metallurgical length." Heat flow models that extend below the mold are needed for basic machine design to ensure that the last support roll and torch cutter are positioned beyond the metallurgical length for the highest casting speed. A heat flow model can also be used to troubleshoot defects. For example, the location of a misaligned support roll that may be generating internal hot-tear cracks can be identified by matching the position of the start of the crack beneath the strand surface with the location of solidification front down the caster calculated with a calibrated model.

5.2.2 Fluid Flow Models

Mathematical models of fluid flow can be applied to many different aspects of the continuous casting process, including ladles, tundishes, nozzles and molds.[12,28] A typical model solves the

following continuity equation and Navier Stokes equations for incompressible Newtonian fluids, which are based on conserving mass (one equation) and momentum (three equations) at every point in a computational domain:[29, 30]

$$\frac{\partial v_i}{\partial x_i} = 0 \qquad \text{(Eq. 5.4)}$$

$$\frac{\partial}{\partial t}\rho v_j + \frac{\partial}{\partial x_i}\rho v_i v_j = -\frac{\partial P}{\partial x_i} + \frac{\partial}{\partial x_i}\mu_{eff}\left(\frac{\partial v_i}{\partial x_i} + \frac{\partial v_j}{\partial x_i}\right) + \alpha(T_0 - T)\rho g_j + F_j \qquad \text{(Eq. 5.5)}$$

where:

$\partial/\partial t$ = differentiation with respect to time (s^{-1}),

ρ = density (kg/m^3),

v_i = velocity component in x_i direction (m/s),

x_i = coordinate direction, x,y, or z (m),

P = pressure field (N/m^2),

μ_{eff} = effective viscosity (kg/m-s),

T = temperature field (K),

T_0 = initial temperature (K),

α = thermal expansion coefficient, (m/m-K),

g_j = magnitude of gravity in j direction (m/s^2),

F_j = other body forces (e.g., from eletromagnetic forces),

i, j = coordinate direction indices; which when repeated in a term, implies the summation of all three possible terms.

The second-to-last term in equation 5.5 accounts for the effect of thermal convection on the flow. The last term accounts for other body forces, such as due to the application of electromagnetic fields. The solution of these equations yields the pressure and velocity components at every point in the domain, which generally should be three-dimensional. At the high flow rates involved in these processes, these models must incorporate turbulent fluid flow. The simplest yet most computationally demanding way to do this is to use a fine enough grid (mesh) to capture all of the turbulent eddies and their motion with time. This method, known as "direct numerical simulation," was used to produce the instantaneous velocity field in the mold cavity of a continuous steel slab caster shown in Fig. 5.4.[7] The 30 seconds of flow simulated to achieve these results on a 1.5 million-node mesh required 30 days of computation on an SGI Origin 2000 supercomputer. The calculations are compared with particle image velocimetry measurements of the flow in a water model, shown on the right side of Fig. 5.4. These calculations reveal structures in the flow pattern that are important to transient events such as the intermittent capture of inclusion particles.

To achieve more computationally-efficient results, turbulence is usually modeled on a coarser grid using a time-averaged approximation, such as the K-ε model,[31] which averages out the effect of turbulence using an increased effective viscosity field, μ_{eff}:

$$\mu_{eff} = \mu_0 + \mu_t = \mu_0 + \rho C_\mu \frac{K^2}{\varepsilon} \qquad \text{(Eq. 5.6)}$$

where:

μ_o , μ_t = laminar and turbulent viscosity fields (kg/m-s),

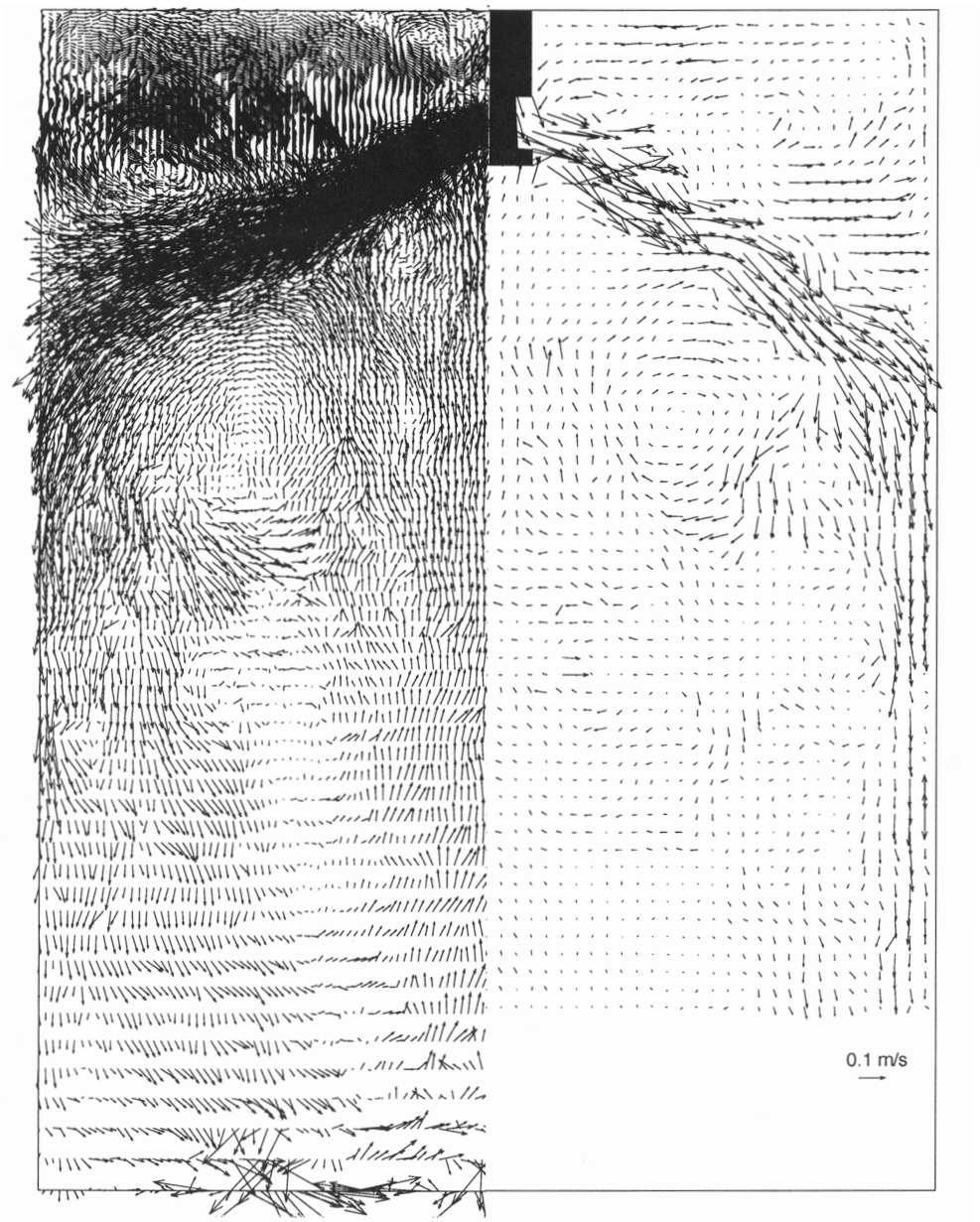

Fig. 5.4 Instantaneous flow pattern in a slab casting mold comparing LES simulation (left) and PIV measurement (right). *From Ref. 7.*

ρ = fluid density (kg/m^3),

C_μ = empirical constant = 0.09,

K = turbulent kinetic energy field, m^2/s^2,

ε = turbulent dissipation field, m^2/s^3.

This approach requires solving two additional partial differential equations for the transport of turbulent kinetic energy and its dissipation:

$$\rho v_j \frac{\partial K}{\partial x_j} = \frac{\partial}{\partial x_j}\left(\frac{\mu_t}{\sigma_K}\frac{\partial K}{\partial x_j}\right) + \mu_t \frac{\partial v_j}{\partial x_i}\left(\frac{\partial v_i}{\partial x_j} + \frac{\partial v_j}{\partial x_i}\right) - \rho\varepsilon \qquad \text{(Eq. 5.7)}$$

$$\rho v_j \frac{\partial \varepsilon}{\partial x_j} = \frac{\partial}{\partial x_j}\left(\frac{\mu_t}{\sigma_\varepsilon}\frac{\partial \varepsilon}{\partial x_j}\right) + C_1 \mu_t \frac{\varepsilon}{K}\frac{\partial v_j}{\partial x_i}\left(\frac{\partial v_i}{\partial x_j} + \frac{\partial v_j}{\partial x_i}\right) - C_2 \frac{\varepsilon}{K}\rho\varepsilon \qquad \text{(Eq. 5.8)}$$

where:

$\partial/\partial x_i$ = differentiation with respect to coordinate direction x,y or z (m),

K = turbulent kinetic energy field, m^2/s^2,

ε = turbulent dissipation field, m^2/s^3,

ρ = density (kg/m^3),

μ_t = turbulent viscosity (kg/m-s),

v_i = velocity component in x, y or z direction (m/s),

σ_K, $\sigma_\times$ = empirical constants (1.0, 1.3),

C_1, C_2 = empirical constants (1.44, 1.92),

i, j = coordinate direction indices, which, when repeated in a term, implies the summation of all three possible terms.

This approach generally uses special "wall functions" as the boundary conditions in order to achieve reasonable accuracy on a coarse grid.[31,32] Alternatively, a "low Reynold's number" turbulence model can be used, which models the boundary layer in a more general way but requires a finer mesh at the walls.[9, 34] An intermediate method between direct numerical simulation and K-ε turbulence models, called "large eddy simulation," uses a turbulence model only at the sub-grid scale.[35]

Most previous flow models have used the finite difference method, owing to the availability of very fast and efficient solution methods.[36] Popular general-purpose codes of this type include CFX,[37] FLUENT,[38] and PHOENICS.[39] Special-purpose codes of this type include MAGMASOFT[40] and PHYSICA,[41] which also solve for solidification and temperature evolution in castings, coupled with mold filling. The finite element method, such as used in FIDAP,[42] can also be applied and has the advantage of being more easily adapted to arbitrary geometries, although it takes longer to execute. Special-purpose codes of this type include PROCAST[43] and CAFE,[44] which are popular for investment casting processes.

Flow in the mold is of great interest because it influences many important phenomena that have far-reaching consequences on strand quality. Some of these phenomena are illustrated in Fig. 5.2. They include the dissipation of superheat by the liquid jet impinging upon the solidifying shell (and temperature at the meniscus), the flow and entrainment of the top-surface powder layers, top-surface contour and level fluctuations, and the entrapment of subsurface inclusions and gas bubbles. Design compromises are needed to simultaneously satisfy the contradictory requirements for avoiding each of these defect mechanisms, as discussed in Chapter 14.

It is important to extend the simulation as far upstream as necessary to provide adequate inlet boundary conditions for the domain of interest. For example, flow calculations in the mold should be preceded by calculations of flow through the submerged entry nozzle. This provides the velocities entering the mold in addition to the turbulence parameters, K and ε. Nozzle geometry greatly affects the flow in the mold and is easy to change, so it is an important subject for modeling.

The flow pattern changes radically with increasing argon injection rate, which requires the solution of additional equations for the gas phase, and knowledge of the bubble size.[6,37,45] The flow pattern and mixing can also be altered by the application of electromagnetic forces, which can either brake or stir the liquid. This can be modeled by solving the Maxwell, Ohm and charge conservation equations for electromagnetic forces simultaneously with the flow model equations.[46] The

great complexity that these phenomena add to the coupled model equations makes these calculations uncertain and a subject of ongoing research.

5.2.3 Superheat Dissipation

An important task of the flow pattern is to deliver molten steel to the meniscus region that has enough superheat during the critical first stages of solidification. Superheat is the sensible heat contained in the liquid metal above the liquidus temperature and is dissipated mainly in the mold.

The transport and removal of superheat is modeled by solving equation 5.2 using the velocities found from the flow model (equations 5.4 to 5.8). The effective thermal conductivity of the liquid is proportional to the effective viscosity, which can be found from the turbulence parameters (K and ε). The solidification front, which forms the boundary to the liquid domain, can be treated in different ways. Many researchers model flow and solidification as a coupled problem on a fixed grid.[25,47,48] Although very flexible, this approach is subject to convergence difficulties and requires a fine grid to resolve the thin, porous mushy zone next to the thin shell.

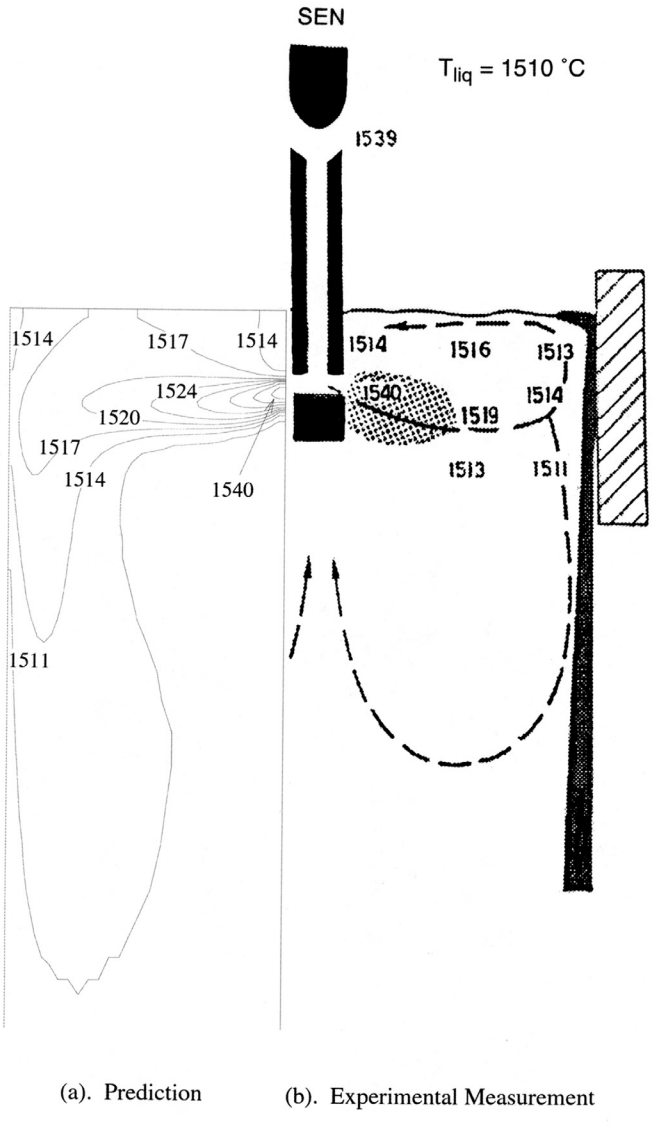

Fig. 5.5 Temperature distribution in mold showing superheat dissipation. *From Ref. 50.*

An alternative approach for columnar solidification of a thin shell, such as found in the mold for the continuous casting of steel, is to treat the boundary as a rough wall fixed at the liquidus temperature using thermal wall laws.[49] Fig. 5.5 compares calculations using this approach with measured temperatures in the liquid pool.[50] Incorporating the effects of argon on the flow pattern was very important in achieving the reasonable agreement observed. This figure shows that the temperature drops almost to the liquidus by mold exit, indicating that most of the superheat is dissipated in the mold. Most of this heat is delivered to the narrow face where the jet impinges, which is important to shell solidification.[51]

The coldest regions are found at the meniscus at the top corners near the narrow face and near the SEN. This is a concern because it could lead to freezing of the meniscus, and encourage solidification of a thick slag rim. This could lead to quality problems such as deep oscillation marks, cracks

and other surface defects. In the extreme, the steel surface can solidify into a solid bridge between the SEN and the shell against the mold wall, which often causes a breakout. To avoid these problems, flow must reach the surface quickly. These calculations should be used, for example, to help design nozzle port geometries that do not direct the flow too deep.

5.2.4 Top Surface Powder/Flux Layer Behavior

The flow of steel in the upper mold may influence the top surface powder layers, which are very important to steel quality. Mold powder is added periodically to the top surface of the steel. It sinters and melts to form a protective liquid flux layer, which helps to trap impurities and inclusions. This liquid is drawn into the gap between the shell and mold during oscillation, where it acts as a lubricant and helps to make heat transfer more uniform. These phenomena are difficult to measure or to accurately simulate with a physical model, so are worthy of mathematical modeling.

Fig. 5.6 shows results from a 3-D finite-element model of heat transfer and fluid flow in the powder and flux layers, based on solving equations 5.2, 5.4 and 5.5.[52] The bottom of the model domain is the steel/flux interface. Its shape is imposed based on measurements in an operating caster. Alternatively, this interface shape can be calculated by solving additional equations to satisfy the force balance at the interface, which involves the pressure in the two phases, shear forces from the moving fluids, surface tension and gravity.[53] For the conditions in this figure, the momentum of the flow up the narrow face has raised the level of the interface there. The shear stress along the interface is determined through coupled calculations with the 3-D steady flow model. The model features different temperature-dependent flux properties for the interior, during sintering before melting, compared with the region near the narrow face mold walls, where the flux resolidifies to form a solid rim.

When molten steel flows rapidly along the steel/flux interface, it induces motion in the flux layer. If the interface velocity becomes too high, then the liquid flux can be sheared away from the interface, become entrained in the steel jet, and be sent deep into the liquid pool to become trapped in the solidifying shell as a harmful inclusion. If the interface velocity increases further, then the interface standing wave becomes unstable, and huge level fluctuations contribute to further problems.

The thickness of the beneficial liquid flux layer is also very important. As shown in the model calculations in Fig. 5.6, the liquid flux layer may become dangerously thin near the narrow face if the steel flow tends to drag the liquid toward the center. This shortage of flux feeding into the gap can lead to air gaps, reduced nonuniform heat flow, thinning of the shell, and longitudinal surface cracks. Quantifying these phenomena requires modeling of both the steel flow and flux layers.

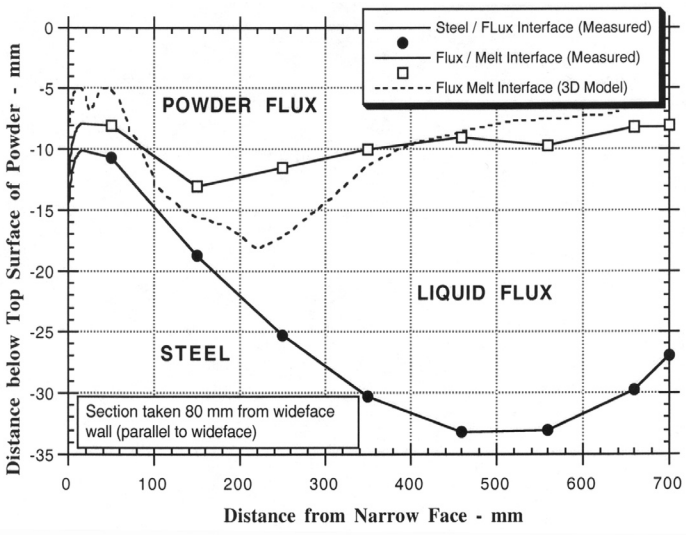

Fig. 5.6 Comparison of measured and predicted melt-interface positions.[52]

5.2.5 Motion and Entrapment of Inclusions and Gas Bubbles

The jets of molten steel exiting the nozzle may carry argon bubbles and inclusions such as alumina into the mold cavity. These particles may create defects if they become entrapped in the solidifying shell. Particle trajectories can be calculated using the Langrangian particle tracking method, which solves a transport equation for each particle as it travels through a previously-calculated velocity field.[34,54,55]

The force balance on each particle includes buoyancy and drag force relative to the molten steel. The effects of turbulent motion can be modeled crudely from a K-ε flow field by adding a random velocity fluctuation at each step, whose magnitude varies with the local turbulent kinetic energy level. To obtain significant statistics, the trajectories of several hundred individual particles should be calculated, using different starting points. The bubbles collect inclusions, and inclusion clusters collide, so their size and shape distributions evolve with time, which affects their drag and flotation velocities and importance. Models are being developed to include these effects.[55]

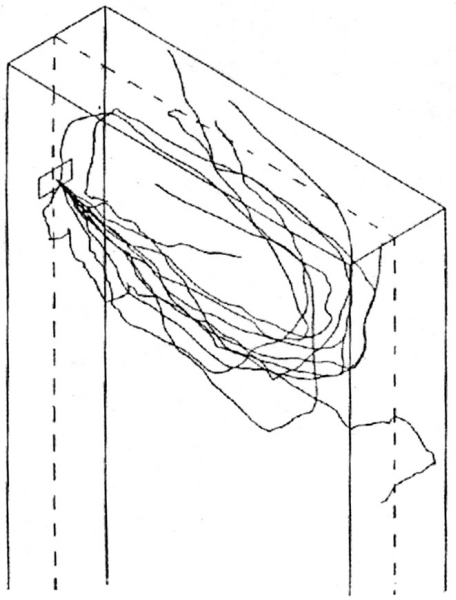

Fig. 5.7 Sample trajectories of 0.3 mm argon bubbles with turbulent motion. *From Ref. 55.*

Fig. 5.7 shows the trajectories of several particles moving through a steady flow field, calculated using the K-ε model.[55] This simulation features particle trajectory tracking that incorporates the influence of turbulence by giving a random velocity component to the velocity at each time step in the calculation, in proportion to the local turbulence level.

Most of the argon bubbles circulate in the upper mold area and float out to the top surface. A few might be trapped at the meniscus if there is a solidification hook, and lead to surface defects. A few small bubbles manage to penetrate into the lower recirculation zone, where they move similarly to large inclusion clusters. Particles in this lower region tend to move slowly in large spirals, while they float toward the inner radius of the slab. When they eventually touch the solidifying shell in this deep region, entrapment is more likely on the inside radius. Trapped argon bubbles elongate during rolling and, in low-strength steel, may expand during subsequent annealing processes to create costly surface blisters and "pencil pipe" defects. Transient models are likely to yield further insights into the complex and important phenomena of inclusion entrapment.

5.2.6 Composition Variation During Grade Changes

Large composition differences can arise through the thickness and along the length of the final product due to intermixing after a change in steel grade during continuous casting. Steel producers need to optimize casting conditions and grade sequences to minimize the amount of steel downgraded or scrapped due to this intermixing. In addition, the unintentional sale of intermixed product must be avoided. To do this requires knowledge of the location and extent of the intermixed region and how it is affected by grade specifications and casting conditions.

Models to predict intermixing must first simulate composition change in both the tundish and in the liquid core of the strand as a function of time. This can be done using simple lumped mixing-box models and/or by solving the mass diffusion equation in the flowing liquid:

$$\frac{\partial C}{\partial t} + v_i \frac{\partial C}{\partial x_i} = \frac{\partial}{\partial x_i}(D_{eff}) \frac{\partial C}{\partial x_i} \qquad \text{(Eq. 5.9)}$$

In this equation, the composition, C, ranges between the old grade concentration of 0 and the new grade concentration of 1. This dimensionless concept is useful because alloying elements intermix essentially equally, owing to the much greater importance of convection and turbulent diffusion D_{eff} over laminar diffusion. In order to predict the composition distribution within the final product, a further model must account for the cessation of intermixing after the shell has solidified.

Fig. 5.8 shows example composition distributions in a continuous cast slab calculated using such a model.[56,57] To ensure accuracy, extensive verification and calibration must be undertaken for each submodel.[57] The tundish mixing submodel must be calibrated to match chemical analysis of steel samples taken from the mold in the nozzle port exit streams, or with tracer studies using full-scale water models. Accuracy of a simplified strand submodel is demonstrated in Fig. 5.8 through comparison both with composition measurements in a solidified slab and with a full 3-D model (equation 5.4).

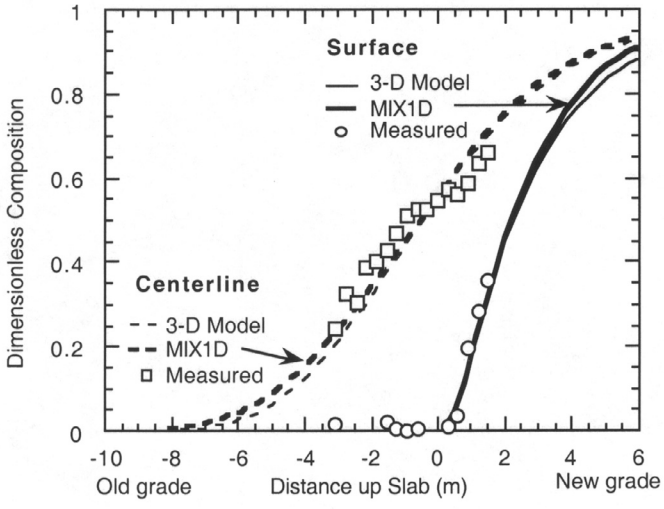

Fig. 5.8 Predicted composition distribution in a steel slab cast during a grade change compared with experiments. *From Ref. 57.*

The results in Fig. 5.8 clearly show the important difference between centerline and surface composition. New grade penetrates deeply into the liquid cavity and contaminates the old grade along the centerline. Old grade lingers in the tundish and mold cavity to contaminate the surface composition of the new grade. This difference is particularly evident in small tundish, thick-mold operations, where mixing in the strand is dominant.

Intermix models such as this one are in use at many steel companies. The model can be enhanced to serve as an on-line tool by outputting, for each grade change, the critical distances that define the length of intermixed steel product that falls outside the given composition specifications for the old and new grades.[57] In addition, it can be applied off-line to perform parametric studies to evaluate the relative effects on the amount of intermixed steel for different intermixing operations and for different operating conditions using a standard ladle-exchange operation.[58] Finally, it can be used to optimize scheduling and casting operation in order to minimize cost.

5.2.7 Thermal Mechanical Behavior of the Mold

Thermal distortion of the mold during operation is important to residual stress, residual distortion, fatigue cracks and mold life. By affecting the internal geometry of the mold cavity, it is also important to heat transfer to the solidifying shell. To study thermal distortion of the mold and its related phenomena first requires accurate solution of heat transfer, equation 5.3, using measurements to help determine the interfacial heat flux. In addition, a thermal-mechanical model must solve the equilibrium equations that relate force and stress, the constitutive equations that relate stress and strain, and the compatibility equations that relate strain and displacement.

$$F_i = \frac{\partial \sigma_{ij}}{\partial x_i} \qquad \text{(Eq. 5.10)}$$

$$\sigma_{ij} = D_{ijkl}\varepsilon_{ij}^{el} \qquad \text{(Eq. 5.11)}$$

$$\varepsilon_{ij}^{tot} = \tfrac{1}{2}\left(\frac{\partial u_i}{\partial x_j} + \frac{\partial u_j}{\partial x_i}\right) \qquad \text{(Eq. 5.12)}$$

where:

$\partial/\partial x$ = differentiation with respect to coordinate direction (m^{-1}),

F_i = force component in i direction (N),

σ_{ij} = stress component (N/m^2),

x_i = coordinate direction, x, y or z (m),

D_{ijkl} = components of elasticity tensor (N/m^2),

ε_{ij}^{el} = elastic strain component (–)

ε_{ij}^{tot} = total strain component (–),

u_i = displacement component in i direction (m),

i = coordinate direction index which, when appearing twice in a term, implies the summation of all three possible terms.

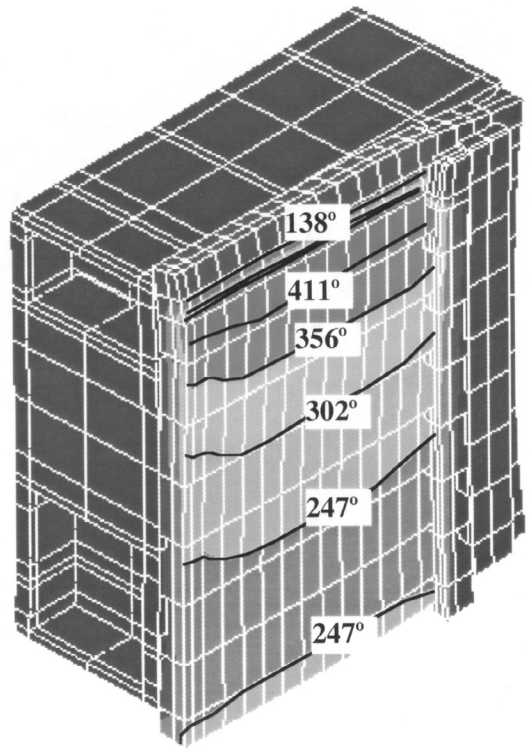

Fig. 5.9 Distorted shape of thin slab casting mold during operation (50X magnification) with temperature contours (°C). *From Ref. 61.*

Thermal strain is found from the temperatures calculated in the heat transfer model and accounts for the difference between the elastic and total strain. Further details are found elsewhere.

In order to match the measured distortion, models should incorporate all the important geometric features of the mold, which often includes the four copper plates with their water slots, reinforced steel water box assemblies, and tightened bolts. Three-dimensional elastic-plastic-creep finite element models have been developed for slabs[59] and thin slabs[60,61] using the commercial finite-element package ABAQUS,[62] which is well suited to this nonlinear thermal stress problem. Their four-piece construction makes slab molds behave very differently from single-piece bloom or billet molds, which have also been studied using thermal stress models.[63]

Fig. 5.9 illustrates typical temperature contours and the displaced shape calculated in one quarter of the mold under steady operating conditions.[61] The hot exterior of each copper plate attempts to expand but is constrained by its colder interior and the cold,

stiff, steel water jacket. This makes each plate bend in toward the solidifying steel. Maximum inward distortions of more than one millimeter are predicted just above the center of the mold faces, and below the location of highest temperature, which is found just below the meniscus.

The narrow face is free to rotate away from the wide face and contact only along a thin vertical line at the front corner of the hot face. This hot edge must transmit all of the clamping forces, so it is prone to accelerated wear and crushing, especially during automatic width changes. If steel enters the gaps formed by this mechanism, this can lead to finning defects or even a sticker breakout. In addition, the wide faces may be gouged, leading to longitudinal cracks and other surface defects.

The high compressive stress due to constrained thermal expansion induces creep in the hot exterior of the copper plates that face the steel. This relaxes the stresses during operation but allows residual tensile stress to develop during cooling. Over time, these cyclic thermal stresses and creep build up significant distortion of the mold plates. This can contribute greatly to remachining requirements and reduced mold life. Under adverse conditions, this stress could lead to cracking of the copper plates. The distortion predictions are important for designing mold taper to avoid detrimental air gap formation.

These practical concerns can be investigated with quantitative modeling studies of the effects of different process and mold design variables on mold temperature, distortion, creep and residual stress. This type of stress model application will become more important in the future to optimize the design of the new molds being developed for continuous thin-slab and strip casting. For example, thermal distortion of the rolls during operation of a twin-roll strip caster is on the same order as the section thickness of the steel product.

5.2.8 Thermal Mechanical Behavior of the Shell

The solidifying shell is prone to a variety of distortion, cracking and segregation problems, owing to its creep at elevated temperature, combined with metallurgical embrittlement and thermal stress. To start to investigate these problems, models are being developed to simulate coupled fluid flow, thermal and mechanical behavior of the solidifying steel shell during continuous casting.[17,60,64] The thermal-mechanical solution procedure is documented elsewhere.[65] In addition to solving equations 5.2, 5.3, 5.10, 5.11 and 5.12, further constitutive equations are needed to characterize the inelastic creep and plastic strains as a function of stress, temperature and structure in order to accurately incorporate the mechanical properties of the material. For example,[66]

$$\dot{\varepsilon}_p = C \exp\left(\frac{-Q}{T}\right)[\sigma - a_\varepsilon \varepsilon_p^{n_\varepsilon}]^n \qquad \text{(Eq. 5.13)}$$

where:

$\dot{\varepsilon}$ = inelastic strain rate (s^{-1}),

σ = stress (MPa),

ε_p = inelastic strain (structure parameter),

T = temperature (K),

$C, Q, a_\varepsilon, n_\varepsilon, n$ = empirical constants.

Constitutive equations such as these are a subject of ongoing research because the equations are difficult to develop, especially for complex loading conditions involving stress reversals. The numerical methods to evaluate them are prone to instability, and the experimental measurements they are based upon are difficult to conduct.

Thermal-mechanical models can be applied in order to predict the evolution of temperature, stress and deformation of the solidifying shell while in the mold for both billets[15] and slabs.[16,67–70] In this region, these phenomena are intimately coupled because the shrinkage of the shell affects heat transfer across the air gap, which complicates the calculation procedure. The predicted temperature contours and distorted shape of a transverse region near the corner are compared in Fig. 5.10 with measurements of a breakout shell from an operating steel caster.[16] This model tracks the behavior of a two-dimensional slice through the strand as it moves downward at the casting speed through the mold and upper spray zones. It consists of separate finite-element models of heat flow and stress generation that are step-wise coupled through the size of the interfacial gap. The heat transfer model was calibrated using thermocouple measurements down the centerline of the wide face for typical conditions. Shrinkage predictions from the stress model are used to find the air gap thickness needed in equation 5.3 in order to extend the calculations around the mold perimeter. The model includes the effect of mold distortion on the air gaps, and superheat delivery from the flowing jet of steel, calculated in separate models. The stress model includes ferrostatic pressure from the molten steel on the inside of the shell and calculates intermittent contact between the shell and the mold. It also features a temperature-dependent elastic modulus and an elastic-viscoplastic constitutive equation that includes the effects of temperature, composition, phase transformations and stress state on the local inelastic creep rate. Efficient numerical algorithms are needed to integrate the equations.

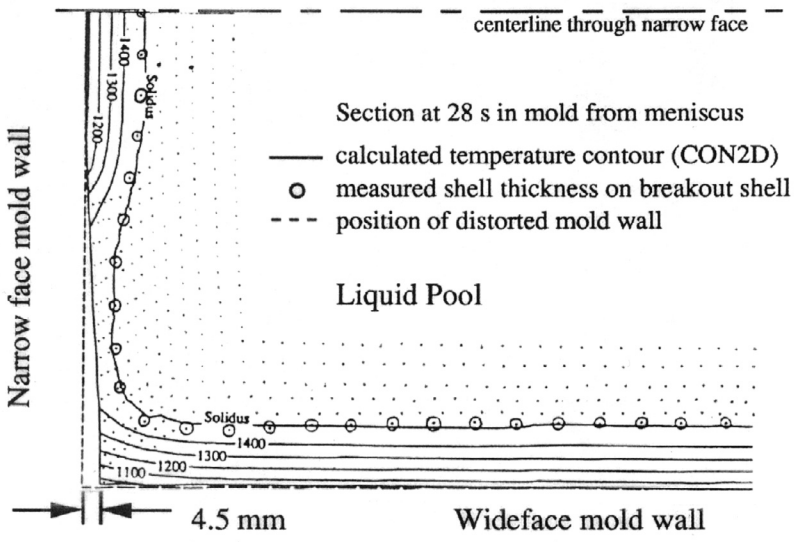

Fig. 5.10 Comparison between predicted and measured shell thickness in a horizontal (x-y) section through the corner of a continuous-cast steel breakout shell. *From Ref. 16.*

As expected, good agreement is obtained in the region of good contact along the wide face, where calibration was done. Near the corner along the narrow face, steel shrinkage is seen to exceed the mold taper, which was insufficient. Thus, an air gap is predicted. This air gap lowers heat extraction from the shell in the off-corner region of the narrow face. When combined with high superheat delivery from the bifurcated nozzle directed at this location, shell growth is greatly reduced locally. Just below the mold, this thin region along the off-corner narrow-face shell caused the breakout.

Near the center of the narrow face, creep of the shell under ferrostatic pressure from the liquid is seen to maintain contact with the mold, so much less thinning is observed. This illustrates the tremendous effect that superheat has on slowing shell growth, if there is a problem that lowers heat flow.

Fig. 5.11 presents sample distributions of temperature and stress through the thickness of the shell, calculated with this model.[70] To achieve reasonable accuracy, a very fine mesh and small time steps are needed. The temperature profile is almost linear through the shell. The stress profile shows that the shell surface is in compression. This is because, in the absence of friction with the mold, the surface layer solidifies and cools stress free. As each inner layer solidifies, it cools and tries to shrink,

while the surface temperature remains relatively constant. The slab is constrained to remain planar, so complementary subsurface tension and surface compression stresses are produced. Note that the average stress through the shell thickness is zero in order to maintain force equilibrium. It is significant that the maximum tensile stress is found near the solidification front. This generic subsurface tensile stress is responsible for hot tear cracks, when accompanied by metallurgical embrittlement.

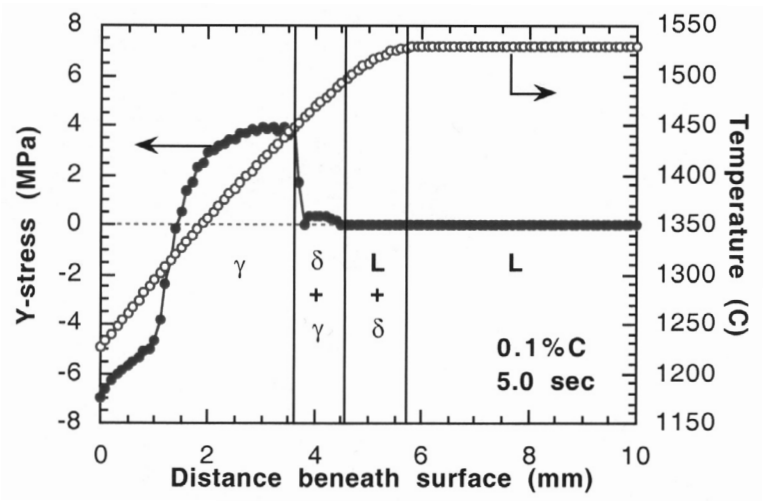

Fig. 5.11 Typical temperature and stress distributions through shell thickness. *From Ref. 70.*

Thermal-mechanical models such as this one can be applied to predict ideal mold taper,[71] to prevent breakouts such as the one discussed here[24] and to understand the cause of other problems such as surface depressions[72] and longitudinal cracks. When combined with transient temperature, flow and pressure calculations in the slag layers, such models can simulate phenomena at the meniscus such as oscillation mark formation.[73]

Computational models can also be applied to calculate thermomechanical behavior of the solidifying shell below the mold. Models can investigate shell bulging between the support rolls due to ferrostatic-pressure induced creep,[74–78] and the stresses induced during unbending.[79] These models are important for the design of spray systems and rolls in order to avoid internal hot tear cracks and centerline segregation. These models face great numerical challenges because the phenomena are generally three-dimensional and transient, the constitutive equations are highly nonlinear, and the mechanical behavior in one region (e.g., the mold) may be coupled with the behavior very far away (e.g., unbending rolls).

5.2.9 Crack Formation

Although obviously of great interest, crack formation is particularly difficult to model directly and is rarely attempted. Very small strains (on the order of 1%) can start hot tear cracks at the grain boundaries if liquid metal is unable to feed through the secondary dendrite arms to accommodate the shrinkage. Strain localization may occur on both the small scale (when residual elements segregate to the grain boundaries) and on a larger scale (within surface depressions or hot spots). Later sources of tensile stress, including constraint due to friction and sticking, unsteady cooling below the mold, withdrawal forces, bulging between support rolls, and unbending all worsen strain concentration and promote crack growth. Microstructure, grain size and segregation are extremely complex, so modeling of these phenomena is generally done independently of the stress model. Of even greater difficulty for computational modeling is the great difference in scale between these microstructural phenomena relative to the size of the casting, where the important macroscopic temperature and stress fields develop.

Considering this complexity, the results of macroscopic thermal-stress models are linked to the microstructural phenomena that control crack initiation and propagation through the use of fracture criteria. To predict hot tear cracks, most fracture criteria identify a critical amount of inelastic strain (e.g., 1 – 3.8%) accumulated over a critical range of liquid fraction, f_L, such as $0.01 < f_L < 0.2$.[80,81] Recent work suggests that the fracture criteria should consider the inelastic strain rate,

which is important during liquid feeding through a permeable region of dendrite arms in the mushy zone.[82] Careful experiments are needed to develop these fracture criteria by applying stress during solidification.[83–85] There experiments are difficult to control, so detailed modeling of the experiment itself is becoming necessary, in order to extract more fundamental material properties such as fracture criteria.

5.2.10 Centerline Segregation

Macrosegregation near the centerline of the solidified slab is detrimental to product properties, particularly for highly alloyed steels, which experience the most segregation. Centerline segregation can be reduced and even avoided through careful application of electromagnetic forces, and soft reduction, where the slab is rolled or quenched just before it is fully solidified. Computational modeling would be useful to understanding and optimizing these practices.

Centerline segregation is a very difficult problem to simulate because such a wide range of coupled phenomena must be properly modeled. Bulging between the rolls and solidification shrinkage together drive the fluid flow necessary for macrosegregation, so fluid flow, solidification heat transfer and stresses must all be modeled accurately (including equations 5.2, 5.4, 5.5, 5.10, 5.12 and 5.13). The microstructure is also important, as equiaxed crystals behave differently than columnar grains, and so must also be modeled. This is complicated by the convection of crystals in the molten pool in the strand, which depends on both flow from the nozzle and thermal/solutal convection. Increasing superheat tends to worsen segregation, so the details of mold superheat transfer must also be properly modeled. Naturally, equation 5.8 must be solved for each important alloying element on both the microstructural scale (between dendrite arms), with the help of microsegregation software such as THERMOCALC,[86] and on the macroscopic scale (from surface to center of the strand), using advanced computations.[48,87] The diffusion coefficients and partition coefficients needed for this calculation are not currently known with sufficient accuracy. Finally, the application of electromagnetic and roll forces generate additional modeling complexity. Although the task appears overwhelming, steps are being taken to model this important problem.[88,89]

Much further work is needed to understand and quantify these phenomena and to apply the results to optimize the continuous casting process. In striving towards these goals, the importance of combining modeling and experiments together cannot be overemphasized.

5.3 Conclusion

The final test of a model is if the results can be implemented and improvements can be achieved, such as the avoidance of defects in the steel product. Plant trials are ultimately needed for this implementation. Trials should be conducted on the basis of insights supplied from all available sources, including physical models, mathematical models, literature and previous experience.

As increasing computational power continues to advance the capabilities of numerical simulation tools, modeling should play an increasing role in future advances to high-technology processes such as the continuous casting of steel. Modeling can augment traditional research methods in generating and quantifying the understanding needed to improve any aspect of the process. Areas where advanced computational modeling should play a crucial role in future improvements include transient flow simulation, mold flux behavior, taper design, online quality prediction and control, especially for new problems and processes such as high-speed billet casting, thin slab casting and strip casting.

Future advances in the continuous casting process will not come from either models, experiments, or plant trials. They will come from ideas generated by people who understand the process and the

problems. This understanding is rooted in knowledge, which can be confirmed, deepened, and quantified by tools that include computational models. As our computational tools continue to improve, they should grow in importance in fulfilling this important role, leading to future process advances.

References

1. J. Szekely, J.W. Evans and J.K. Brimacombe, *The Mathematical and Physical Modeling of Primary Metals Processing Operations* (New York: John Wiley & Sons, 1987).
2. J. Szekely and N. Themelis, *Rate Phenomena in Process Metallurgy* (New York: Wiley-Interscience, 1971), 515–597.
3. R.I.L. Guthrie, *Engineering in Process Metallurgy* (Oxford, UK: Clarendon Press, 1992), 528.
4. L.J. Heaslip and J. Schade, "Physical Modeling and Visualization of Liquid Steel Flow Behavior During Continuous Casting," *Iron & Steelmaker*, 26:1 (1999): 33–41.
5. S.L. Lee, "Particle Drag in a Dilute Turbulent Two-Phase Suspension Flow," *Journal of Multiphase Flow,* 13:2 (1987): 247.
6. B.G. Thomas, X. Huang and R.C. Sussman, "Simulation of Argon Gas Flow Effects in a Continuous Slab Caster," *Metall. Trans.* B, 25B:4 (1994): 527–547.
7. S. Sivaramakrishnan, H. Bai, B.G. Thomas, P. Vanka, P. Dauby and M. Assar, "Transient Flow Structures in Continuous Cast Steel," in *Ironmaking Conference Proceedings,* 59, Pittsburgh, Pa. (Warrendale, Pa.: Iron and Steel Society, 2000), 541–557.
8. M.B. Assar, P.H. Dauby and G.D. Lawson, "Opening the Black Box: PIV and MFC Measurements in a Continuous Caster Mold," in *Steelmaking Conference Proceedings,* 83 (Warrendale, Pa.: Iron and Steel Society, 2000), 397–411.
9. X.K. Lan, J.M. Khodadadi and F. Shen, "Evaluation of Six k-Turbulence Model Predictions of Flowin a Continuous Casting Billet-Mold Water Model Using Laser Doppler Velocimetry Measurements," *Metall. Mater. Trans.,* 28B:2 (1997): 321–332.
10. J. Herbertson, Q.L. He, P.J. Flint and R.B. Mahapatra, "Modelling of Metal Delivery to Continuous Casting Moulds," in *Steelmaking Conference Proceedings,* 74 (Warrendale, Pa.: Iron and Steel Society, 1991), 171–185.
11. B.G. Thomas, R. O'Malley, T. Shi, Y. Meng, D. Creech and D. Stone, "Validation of Fluid Flow and Solidification Simulation of a Continuous Thin Slab Caster," in *Modeling of Casting, Welding, and Advanced Solidification Processes, IX,* Aachen, Germany, Aug. 20–25, 2000 (Aachen, Germany: Shaker Verlag GmbH, 2000), 769–776.
12. B.G. Thomas, "Mathematical Modeling of the Continuous Slab Casting Mold: A State of the Art Review," in *74th Steelmaking Conference Proceedings,* 74 (Warrendale, Pa.: Iron and Steel Society, 1991), 105–118.
13. J. Lait, J.K. Brimacombe and F. Weinberg, "Mathematical Modelling of Heat Flow in the Continuous Casting of Steel," *Ironmaking and Steelmaking,* 2 (1974): 90–98.
14. R.B. Mahapatra, J.K. Brimacombe and I.V. Samarasekera, "Mold Behavior and its Influence on Quality in the Continuous Casting of Slabs: Part I. Industiral Trials, Mold Temperature Measurements, and Mathematical Modelling," *Metallurgical Transactions B*, 22B (Dec. (1991), 861–874.
15. J.E. Kelly, K.P. Michalek, T.G. OConnor, B.G. Thomas, J.A. Dantzig, "Initial Development of Thermal and Stress Fields in Continuously Cast Steel Billets," *Metallurgical Transactions A,* 19A:10 (1988): 2589–2602.
16. A. Moitra and B.G. Thomas, "Application of a Thermo-Mechanical Finite Element Model of Steel Shell Behavior in the Continuous Slab Casting Mold," in *Steelmaking Proceedings,* 76 (Dallas, Texas: Iron and Steel Society, 1993), 657–667.
17. J.-E. Lee, T.-J. Yeo, K.H. Oh, J.-K. Yoon and U.-S. Yoon, "Prediction of Cracks in Continuously Cast Beam Blank Through Fully Coupled Analysis of Fluid Flow, Heat Transfer and Deformation Behavior of Solidifying Shell," *Metall. Mater. Trans. A,* 31A:1 (2000): 225–237.

18. R. Bommaraju and E. Saad, "Mathematical modelling of lubrication capacity of mold fluxes," in *Steelmaking Proceedings,* 73 (Warrendale, Pa.: Iron and Steel Society, 1990), 281–296.
19. B.G. Thomas and B. Ho, "Spread Sheet Model of Continuous Casting," *J. Engineering Industry,* 118:1 (1996): 37–44.
20. B. Ho, "Characterization of Interfacial Heat Transfer in the Continuous Slab Casting Process" (Masters Thesis, University of Illinois at Urbana–Champaign, 1992).
21. J.A. DiLellio and G.W. Young, "An Asymptotic Model of the Mold Region in a Continuous Steel Caster," *Metall. Mater. Trans.,* 26B:6 (1995): 1225–1241.
22. B.G. Thomas, D. Lui and B. Ho, "Effect of Transverse and Oscillation Marks on Heat Transfer in the Continuous Casting Mold," in *Applications of Sensors in Materials Processing,* edited by V. Viswanathan, Orlando, Fla. (Warrendale, Pa.: TMS, 1997), 117–142.
23. B.G. Thomas, B. Ho and G. Li, "Heat Flow Model of the Continuous Slab Casting Mold, Interface, and Shell," in *Alex McLean Symposium Proceedings,* Toronto (Warrendale, Pa.: Iron and Steel Society, 1998), 177–193.
24. G.D. Lawson, S.C. Sander, W.H. Emling, A. Moitra and B.G. Thomas, "Prevention of Shell Thinning Breakouts Associated with Widening Width Changes," in *Steelmaking Conference Proceedings,* 77 (Warrendale, Pa.: Iron and Steel Society, 1994), 329–336.
25. C.-A. Gandin, T. Jalanti and M. Rappaz, "Modeling of Dendritic Grain Structures," in *Modeling of Casting, Welding, and Advanced Solidification Processes,* VIII, edited by B.G. Thomas and C. Beckermann (Warrendale, Pa.: TMS, 1998), 363–374.
26. I. Steinbach and G.J. Schmitz, "Direct Numerical Simulation of Solidification Structure using the Phase Field Method," in *Modeling of Casting, Welding, and Advanced Solidification Processes,* VIII, edited by B.G. Thomas and C. Beckermann (Warrendale, Pa.: TMS, 1998), 521–532.
27. R.A. Hardin, K. Liu and C. Beckermann, "Development of a Model for Transient Simulation and Control of a Continuous Steel Slab Caster," in *Materials Processing in the Computer Age, 3* (Warrendale, Pa.: Minerals, Metals, & Materials Society, 2000), 61–74.
28. J. Szekely and R.T. Yadoya, "The Physical and Mathematical Modelling of the Flow Field in teh Mold Region of Continuous Casitng Units. Part II. Computer Solution of the Turbulent Flow Equations," *Metall. Mater. Trans.,* 4 (1973): 1379.
29. S.V. Patankar, *Numerical Heat Transfer and Fluid Flow* (New York: McGraw Hill, 1980).
30. S.V. Patankar and B.D. Spalding, "A calculation procedure for heat, mass and momentum transer in three-dimensional parabolic flows," *Int. J. Heat Mass Transfer,* 15 (1992): 1787-1806.
31. B.E. Launder and D.B. Spalding, "Numerical Computation of Turbulent Flows," *Computer Methods in Applied Mechanics and Engr,* 13 (1974): 269–289.
32. B.G. Thomas and F.M. Najjar, "Finite-Element Modeling of Turbulent Fluid Flow and Heat Transfer in Continuous Casting," *Applied Mathematical Modeling,* 15 (1991): 226–243.
33. D.E. Hershey, B.G. Thomas and F.M. Najjar, "Turbulent Flow through Bifurcated Nozzles," *International Journal for Numerical Methods in Fluids,* 17 (1993): 23–47.
34. M.R. Aboutalebi, M. Hasan and R.I.L. Guthrie, "Coupled Turbulent Flow, Heat, and Solute Transport in Continuous Casting Processes," *Metall. Mater. Trans.,* 26B:4 (1995): 731–744.
35. J. Smagorinsky, "General Circulation Experiments with the Primitive Equations" (Washington: Report, Weather Bureau, 1963), 99–121.
36. N.C. Markatos, "Computational Fluid Flow Capabilities and Software," *Ironmaking and Steelmaking,* 16:4 (1989): 266–273.
37. "CFX 4.2" (Pittsburgh, Pa.: AEA Technology, 1998).
38. "FLUENT 5.1" (Lebanon, N.H.: Fluent Inc., 2000).
39. "PHOENICS" (London: CHAM, 2000).
40. E. Flender, "MAGMASOFT" (Aachen, Germany: Magma Gmbh, 2000).
41. M. Cross, "PHYSICA" (Greenwich, UK: Computing & Math Sciences, 2000).
42. M.S. Engleman, "FIDAP 8.5" (Evanston, Ill.: Fluent, Inc., 2000).
43. M. Sammonds, "PROCAST" (Annapolis, Md.: UES Software, 2000).
44. P. Thevoz, "CAFE" (Lausanne, Switzerland: CALCOM, EPFL, 2000).

45. N. Bessho, R. Yoda, H. Yamasaki, T. Fujii and T. Nozaki, "Numerical Analysis of Fluid Flow in the Continuous Casting Mold by a Bubble Dispersion Model," *Iron and Steelmaker,* 18:4 (1991): 39–44.
46. T. Ishii, S.S. Sazhin and M. Makhlouf, "Numerical prediction of magnetohydrodynamic flow in continuous casting process," *Ironmaking and Steelmaking,* 23:3 (1996): 267–272.
47. V.R. Voller, A.D. Brent and C. Prakash, "The Modelling of Heat, Mass and Solute Transport in Solidification Systems," *Applied Mathematical Modelling,* 32 (1989): 1719–1731.
48. M.C. Schneider and C. Beckermann, "The Formation of Macrosegregation by Multicomponent Thermosolutal Convection During the Solidification of Steel," *Metall. Mater. Trans. A,* 26A (1995): 2373–2388.
49. X. Huang, B.G. Thomas and F.M. Najjar, "Modeling Superheat Removal During Continuous Casting of Steel Slabs," *Metallurgical Transactions B,* 23B:6 (1992): 339–356.
50. B.G. Thomas, "Continuous Casting of Steel, Chap. 15," in *Modeling and Simulation for Casting and Solidification: Theory and Applications,* edited by O. Yu (New York: Marcel Dekker, 2000).
51. H. Nakato, M. Ozawa, K. Kinoshita, Y. Habu and T. Emi, "Factors Affecting the Formation of Shell and Longitudinal Cracks in Mold During High-Speed Continuous Casting of Slabs," *Trans. Iron Steel Inst. Japan,* 24:11 (1984): 957–965.
52. R. McDavid and B.G. Thomas, "Flow and Thermal Behavior of the Top-Surface Flux/Powder Layers in Continuous Casting Molds," *Metallurgical Transactions B,* 27B:4 (1996): 672–685.
53. G.A. Panaras, A. Theodorakakos and G. Bergeles, "Numerical Investigation of the Free Surface in a continuous Steel Casting Mold Model," *Metall. Mater. Trans. B,* 29B (5) (1998): 1117–1126.
54. R.C. Sussman, M. Burns, X. Huang and B.G. Thomas, "Inclusion Particle Behavior in a Continuous Slab Casting Mold," in *10th Process Technology Conference Proc.,* 10, Toronto (Warrendale, Pa.: Iron and Steel Society, 1992), 291–304.
55. B.G. Thomas, A. Dennisov and H. Bai, "Behavior of Argon Bubbles During Continuous Casting of Steel," in *Steelmaking Conference Proceedings,* 80, Chicaago (Warrendale, Pa.: Iron and Steel Society, 1997), 375–384.
56. X. Huang and B.G. Thomas, "Modeling of Steel Grade Transition in Continuous Slab Casting Processes," *Metallurgical Transactions,* 24B (1993): 379–393.
57. X. Huang and B.G. Thomas, "Intermixing Model of Continuous Casting During a Grade Transition," *Metallurgical Mater Transactions B,* 27B:4 (1996): 617–632.
58. B.G. Thomas, "Modeling Study of Intermixing in Tundish and Strand During a Continuous-Casting Grade Transition," *ISS Transactions,* 24:12 (1997): 83–96.
59. B.G. Thomas, G. Li, A. Moitra and D. Habing, "Analysis of Thermal and Mechanical Behavior of Copper Molds during Continuous Casting of Steel Slabs," *Iron and Steelmaker (ISS Transactions),* 25:10 (1998): 125–143.
60. T. O'Conner and J. Dantzig, "Modeling the Thin Slab Continuous Casting Mold," *Metall. Mater. Trans.,* 25B:4 (1994): 443–457.
61. J.-K. Park, I.V. Samarasekera, B.G. Thomas and U.-S. Yoon, "Analysis of Thermal and Mechanical Behavior of Copper Mould During Thin Slab Casting," in *Steelmaking Conference Proceedings,* 83 (Warrendale, Pa.: Iron and Steel Society, 2000), 9–21.
62. "ABAQUS 5.8" (Pawtucket, R.I.: Hibbitt, Karlsson & Sorensen, Inc., 1999).
63. I.V. Samarasekera, D.L. Anderson and J.K. Brimacombe, "The Thermal Distortion of Continuous Casting Billet Molds," *Metallurgical Transactions B,* 13B (March 1982): 91–104.
64. A. Cristallini, M.R. Ridolfi, A. Spaccarotella, R. Capotosti, G. Flemming and J. Sucker, "Advanced Process Modeling of CSP Funnel Design for Thin Slab Casting of High-Alloyed Steels," in *Seminario de Aceria of the Instituto Argentino de Siderurgia (IAS) Proceedings,* (Buones Aires, Argentina: IAS, 1999), 468–477.
65. J.A. Dantzig, "Thermal Stress Development in Metal Casting Processes," *Metallurgical Science and Technology,* 7:3 (1989): 133–178.
66. P. Kozlowski, B.G. Thomas, J. Azzi and H. Wang, "Simple Constitutive Equations for Steel at High Temperature," *Metallurgical Transactions A,* 23A (March 1992): 903–918.
67. K. Sorimachi and J.K. Brimacombe, "Improvements in Mathematical Modelling of Stresses in Continuous Casting of Steel," *Ironmaking and Steelmaking,* 4 (1977): 240–245.

68. K. Kinoshita, H. Kitaoka and T. Emi, "Influence of Casting Conditions on the Solidification of Steel Melt in Continuous Casting Mold," *Tetsu-to-Hagane,* 67:1 (1981): 93–102.
69. I. Ohnaka and Y. Yashima, "Stress Analysis of Steel Shell Solidifying in Continuous Casting Mold," in *Modeling of Casting and Welding Processes IV*, 4 (Warrendale, Pa.: Minerals, Metals, and Materials Society, 1988), 385–394.
70. B.G. Thomas and J.T. Parkman, "Simulation of Thermal Mechanical Behavior During Initial Solidification," in *Thermec 97 Internat. Conf. on Thermomechanical Processing of Steel and Other Materials,* 2, edited by T. Chandra (Wollongong, Australia: TMS, 1997), 2279–2285.
71. B.G. Thomas, A. Moitra and W.R. Storkman, "Optimizing Taper in Continuous Slab Casting Molds Using Mathematical Models," in *Proceedings, 6th International Iron and Steel Congress,* 3, Nagoya, Japan (Tokyo: Iron & Steel Inst. Japan, 1990), 348–355.
72. B.G. Thomas, A. Moitra and R. McDavid, "Simulation of Longitudinal Off-Corner Depressions in Continuously-Cast Steel Slabs," *ISS Transactions,* 23:4 (1996): 57–70.
73. K. Schwerdtfeger and H. Sha, "Depth of Oscillation Marks Forming in Continuous Casting of Steel," *Metallurgical and Materials Transactions A,* in press (1999).
74. A. Palmaers, A. Etienne and J. Mignon, "Calculation of the Mechanical and Thermal Stresses in Continuously Cast Strands, in German," *Stahl und Eisen,* 99:19 (1979): 1039–1050.
75. J.B. Dalin and J.L. Chenot, "Finite Element Computation of Bulging in Continuously Cast Steel with a Viscoplastic Model," *International Journal for Numerical Methods in Engineering,* 25 (1988): 147–163.
76. B. Barber and A. Perkins, "Strand Deformation in Continuous Casting," *Ironmaking and Steelmaking,* 16:6 (1989): 406–411.
77. K. Okamura and H. Kawashima, "Calculation of Bulging Strain and Its Application to Prediction of Internal Cracks in Continuously Cast Slabs," in *Proc. Int. Conf. Comp. Ass. Mat. Design Proc. Simul.* (Tokyo: ISIJ, 1993), 129–134.
78. L. Yu, "Bulging in Continuous Cast Steel Slabs" (M.S. Thesis, University of Illinois, 2000).
79. M. Uehara, I.V. Samarasekera and J.K. Brimacombe, "Mathematical modelling fo unbending of continuously cast steel slabs," *Ironmaking and Steelmaking,* 13:3 (1986), 138.
80. T.W. Clyne and G.J. Davies, "The influence of composition on solidification cracking susceptibiltity in binary alloy systems," *Br. Foundrymen,* 74:4 (1981): 65–73.
81. A. Yamanaka, K. Nakajima and K. Okamura, "Critical strain for internal crack formation in continuous casting," *Ironmaking and Steelmaking,* 22:6 (1995): 508–512.
82. M. Rappaz, J.-M. Drezet and M. Gremaud, "A New Hot-Tearing Criterion," *Metall. Mater. Trans. A,* 30A:2 (1999): 449–455.
83. T. Matsumiya, M. Ito, H. Kajioka, S. Yamaguchi, Y. Nakamura, "An Evaluation of Critical Strain for Internal Crack Formation in Continuously Cast Slabs," *Transactions of the Iron and Steel Institute of Japan,* 26 (1986): 540–546.
84. C. Bernhard, H. Hiebler and M.M. Wolf, "Experimental simulation of subsurface crack formation in continuous casting," *Rev. Metall.* (March 2000), 333–344.
85. C.H. Yu, M. Suzuki, H. Shibata, T. Emi, "Simulation of Crack Formation on Solidifying Steel Sheel in Continuous Casting Mold," *ISIJ International,* 36 (1996): S159–S162.
86. B. Sundman, B. Jansson and J.O. Anderson, "The Thermo-Calc Databank System," *CALPHAD* 9, 2 (1985): 153–190.
87. C.Y. Wang and C. Beckermann, "Equiaxed Dendritic Solidification with Convection," *Metall. Mater. Trans. A,* 27A:9 (1996): 2754–2764.
88. T. Kajitani, J.-M. Drezet and M. Rappaz, "Numerical simulation of deformation-induced segregation in continuous casting of steel," *Metall. Mater. Trans.* (2001), in press.
89. G. Lesoult and S. Sella, *Solid State Phenomena,* 3 (1988): 167–178.

